

Understanding the Feasibility of Using NiTi55 Interlayer for Ti6Al4V-18Ni Maraging Steel Multi-Metal Deposition in L-PBF

Vinay Kenny^a, Salil Bapat^a, Ajay Malshe^{a,*}

^a Manufacturing and Materials Research Laboratories (MMRL), Purdue University, West Lafayette, IN, 47906.

* Corresponding author: amalshe@purdue.edu.

ABSTRACT

This research is focused on understanding the feasibility of using NiTi55 interlayer for achieving interfacial integrity in the multi-metal deposition of Ti6Al4V (Ti64)-18Ni maraging steel (18NiMS) using laser-assisted powder bed fusion (L-PBF). Achieving proper interfacial integrity in multi-metal systems is a significant challenge, particularly with metal alloys having limited chemical compatibility, such as Ti64 and 18NiMS. Test structures were manufactured by printing Ti64 onto an additively manufactured 18NiMS base pad with and without NiTi55 interlayer. The scanning electron microscopy and energy dispersive X-ray spectroscopy analysis revealed that the addition of the interlayer resulted in reduced defect density in the interfacial zone. X-ray diffraction analysis confirmed the favorable change in intermetallic phases at the multi-metal interface, while electron backscatter diffraction microstructural characterization revealed the intermetallic phase formation and the effect of thermal conductivities on grain size evolution. The reduced interfacial defect density and the replacement of detrimental Fe-Ti with less detrimental Fe-Ni and Ni-Ti intermetallic compounds demonstrated the potential for using NiTi55 interlayer chemistry to improve interfacial integrity in the Ti64-18NiMS system for potential applications such as lightweighting.

Keywords: hybrid manufacturing; multi-metal; laser-powder bed fusion (L-PBF); Ti6Al4V; 18Ni maraging steel.

1. Introduction

The additive manufacturing (AM) of multi-metal (MM) has gained significant traction across various industries due to its ability to produce high-performance parts [1,2]. Critical applications, such as lightweighting, require the strategic combination of a lightweight reactive (R) metal with a dense non-reactive (NR) metal to meet function-specific requirements. One such example is combining Ti6Al4V (Ti64, density - 4.43 g/cc) and 18Ni maraging steel (18NiMS, density - 8 g/cc), both of which are extensively used in high-strength applications [3,4]. However,

ensuring interfacial integrity for MM systems involving ferrous and titanium alloys poses significant challenges due to differences in their chemical, thermal, and mechanical properties, leading to the delamination and warping of parts [5]. As an example, previous reports involving deposition of SS316 over Ti64 using the directed energy deposition (DED) process resulted in delamination due to the combined effect of process-induced residual stresses and the formation of brittle Fe-Ti intermetallic compounds (IMCs) [6]. The formation of these IMCs is due to the limited solid solubility between Ti and Fe [7]. In literature, interlayers such as copper, nickel, and vanadium alloys have been utilized to prevent the local interactions between Fe and Ti at the interface. Although these interlayers reduced interfacial defects, cracking at the interfaces was still observed [8–10]. This is because not a single element possesses sufficient solid solubility with both Ti and Fe, and introducing an interlayer resulted in the formation of new IMCs; hence, the cracked interfaces [11]. This indicated that even though the approach of using various interlayers holds promise, further research is necessary to identify the appropriate interlayer chemistries and processing conditions.

This research is focused on understanding the feasibility of using NiTi55 (nitinol) as an interlayer to promote interfacial integrity between Ti64 and 18NiMS using laser-assisted powder bed fusion (L-PBF) aimed toward lightweighting applications. As a research hypothesis, nitinol was chosen as an interlayer because of the potentially favorable material chemistry of nitinol with maraging steel (containing 18% Ni) and Ti64 (containing 88% Ti). This choice was further supported by the solid solubility in the respective phase diagrams [12,13]. Furthermore, L-PBF with nitinol has been successfully demonstrated in previous reports, with AM-suitable alloy powder being commercially available [14,15]. The nitinol composition, which consists of 55 wt.% nickel and 45 wt.% titanium (equivalent to 50 atomic percent of each element), was chosen as a reasonable initial composition for the interlayer. The novelty of this research lies in the chosen interlayer chemistry and the use of L-PBF as the additive manufacturing equipment for this MM system. This is the first time nitinol interlayer composition has been studied. The interlayer chemistry is partially compatible with Ti and Fe and allows for a gradual transition in titanium concentration in the build direction, resulting in a gradient composition. Additionally, no existing research demonstrates the feasibility of MM deposition of Ti and Fe alloys using L-PBF, which, in most cases, induces less thermal stress in the build part than DED, resulting in better print quality [16,17]. In another unique approach from a production perspective, two different L-PBF setups were utilized, with the ability to handle R and NR material powders, respectively, to mitigate the material handling challenges of these materials and avoid material changeovers.

The following sections discuss the experimental methods and design/manufacturing of the test structures to study the MM interface, followed by characterization results and their discussion. The paper concludes by providing key learnings and scope for future directions.

2. Materials and methods

2.1. Feedstock powder and base plate

Spherical powders of 18NiMS (Matsuura USA), Ti64 (Renishaw), and nitinol (Heeger Materials) were utilized in the study. The particle size distribution exhibited a Gaussian profile, with particle size ranges of 15–45 μm for 18NiMS, 20–45 μm for Ti64, and 15–53 μm for nitinol as per manufacturer specifications. Fig. 1 shows the scanning electron microscope (SEM) images of the feedstock materials. The chemical composition of the powders is listed in Tab. 1. A36 steel base plate (surface ground) of size 125 by 125 mm^2 with a thickness of 10 mm was employed as the substrate due to its thermal and chemical compatibility with 18NiMS.

Table 1: Chemical composition of the feedstock powders.

18NiMS	Fe	Ni	Co	Mo	Ti	Cr	Mn	Si	Al	C
Wt. %	67	18	8.5	4.5	0.6	≤ 0.3	≤ 0.1	≤ 0.1	0.05	≤ 0.03
Ti64	Ti	Al	V	Fe	O	C	N	H	Y	
Wt. %	88	6.75	4.5	0.3	0.2	0.08	0.05	0.015	0.005	
NiTi55	Ni	Ti	C							
Wt. %	55	44.2	0.8							

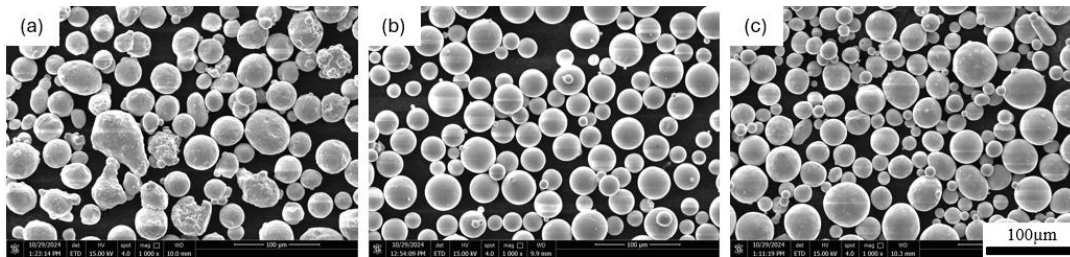


Fig. 1. SEM image of powdered feedstock (a) 18 Ni maraging steel, (b) Ti6Al4V and (c) NiTi55.

2.2. Manufacturing of test structures

Matsuura Lumex Avance 25 hybrid AM systems (with R and NR powder processing capabilities separately) equipped with a 1070 nm Yb fiber laser were employed for the deposition process. The hybrid AM systems are equipped with L-PBF and micro-milling capabilities. The NR system was utilized to print 18NiMS within an inert nitrogen atmosphere, while the R system, operating in an inert argon atmosphere, was used to process Ti64 and nitinol powders.

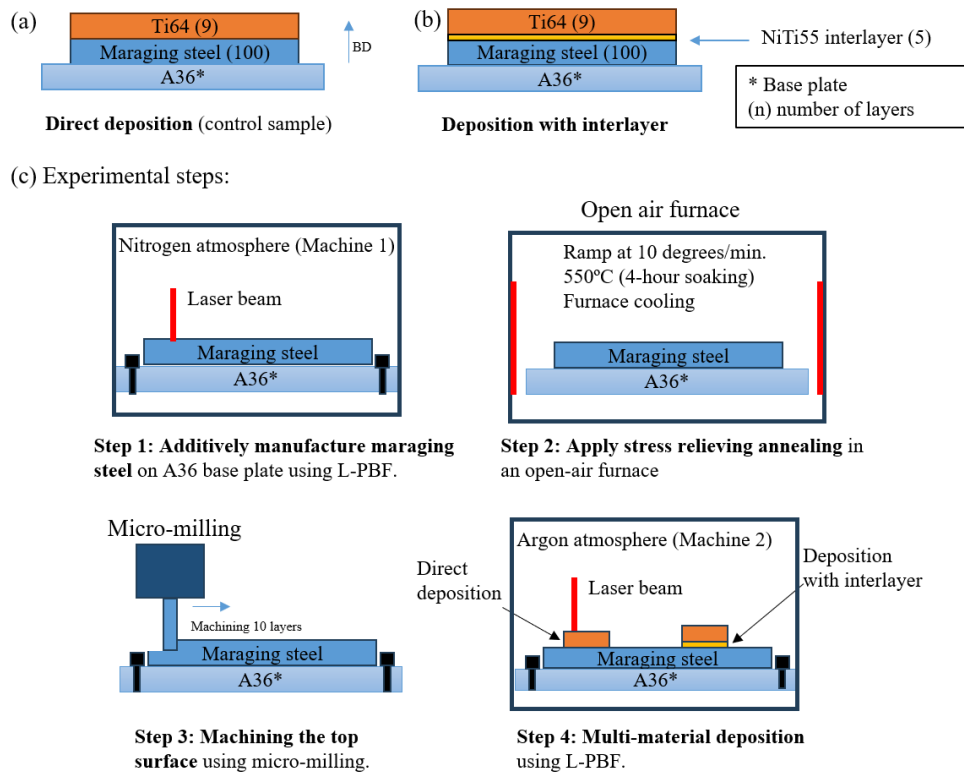


Fig. 2. Experimental test structure (a) direct deposition and (b) deposition with interlayer; (c) experimental steps.

This study included the fabrication of two distinct test structures for comparative analysis: (i) direct deposition, where Ti64 was printed directly onto 18NiMS without any interlayer chemistry, and (ii) deposition with an interlayer, where nitinol was first printed onto 18NiMS, followed by the deposition of Ti64 on top of the nitinol interlayer, as schematically illustrated in Fig. 2 (a and b). Table 2 lists the parameters used for printing individual metal alloys in the MM structure, where ‘d’ is the laser spot diameter, ‘P’ is the laser power, ‘v’ is the scan speed, ‘h’ is the hatch spacing, ‘t’ is the layer thickness, and ‘VED’ is the volumetric energy density which is the ratio of power to the product of speed, hatch and layer thickness. These parameters were based on preliminary experiments to identify the operational window for process parameters of all three metal alloys. This set of parameters resulted in deposition without delamination. For the purpose of this study, the laser parameters were kept constant throughout the experiment to focus on studying the role of interlayer chemistry towards the MM deposition and not on optimization of printing process parameters.

Table 2: Process parameters for the MM deposition.

	d (μM)	P (W)	v (MM/S)	h (μM)	t (μM)	VED (J/MM³)
18NiMS	200	400	500	150	50	106
Ti-64	200	400	500	200	50	80
NITINOL	200	400	500	100	50	160

Fig. 2 (c) shows the schematic illustration of the experimental procedure. 18NiMS pads (100 by 120 mm²) with a thickness of 5mm (100 layers) were first printed on an A36 base plate in an NR machine. From here onwards, this geometry is referred to as base pads, as they represent a common first step for both comparative test structures. After printing, stress-relieving annealing was performed to reduce the residual stresses induced by the printing process. This involved heating the component in an open-air furnace at a rate of 10°C/min until it reached 550°C, holding it at that temperature for 4 hours, and then cooling it to room temperature in the furnace [18]. Afterward, the base plate with the deposited maraging base pad was transferred to the reactive unit, where 10 layers, equivalent to 0.5 mm, were milled off to create a flat surface for uniform layering in preparation for the final deposition steps.

In direct deposition, nine layers of Ti64 were printed on a heat-treated 18NiMS base pad in the form of square coupons with dimensions of 10x10 mm². The deposition was stopped at a step where visual delamination was observed, causing an interference with the recoater blade. These were then allowed to cool by turning off the table heater. For test structures with nitinol interlayer, a separate base pad was used. First, five layers of nitinol with dimensions of 10x10 mm² were printed on top of the heat-treated and machined 18NiMS base pad, and the prints were allowed to cool to room temperature in the printing chamber. The nitinol powder was delivered using a recoater blade to prevent a full machine clean-out, which restricted the number of printed nitinol layers to five. Subsequently, the chamber was opened for powder changeover to Ti64, and nine layers of Ti64 were printed on the nitinol interlayer and allowed to cool to room temperature by turning off the table heat.

All printing operations were carried out at <0.1% chamber oxygen, a table temperature of 50°C, and utilizing an XY scan strategy. Using two separate L-PBF machines helped expedite the processing time without full powder cleanout, while also being able to handle the powdered materials based on their reactivity. All samples were printed in replicates of three and characterized to study the surface morphology and interfacial integrity. The details of the characterization process and methods are briefly summarized below.

2.3. Characterization details

Printed samples were characterized with various microscopic techniques, including SEM, Energy Dispersive X-ray Spectroscopy (EDS), X-ray Diffraction (XRD), and Electron Backscatter Diffraction (EBSD). Specifically, morphological characterization was performed with SEM (SEM, Quanta 650), while chemical mapping was done using EDS (Oxford Instruments Ultim Max 100). Microstructural details, including grain shape, were analyzed with the EBSD (Oxford Instruments Symmetry S3 with Helios G4 SEM). Phase information was determined using XRD (PANalytical X'pert Pro). Both the top surface (as printed) and the cross-sectional profile (for interface characterization) were studied. Briefly, the metallographic sample preparation procedure involved sectioning the printed samples of interest using an alumina cutting wheel (Leco VC-50) at 400 rpm with water as the cutting fluid. All the sectioned samples were later polished using 320, 400, 600, 800, and 1200 grit papers, followed by diamond 6, 3, and 1-micron paste to achieve a mirror finish. The samples were further polished with a vibratory polisher (Pace Technologies GIGA-S) with SIAMAT 2 (Pace Technologies) colloidal silica for 4 hours to reveal the microstructure for EBSD analysis. The experimental results, key observations, and trends are presented below, along with the discussion for process mechanisms and interpretations.

3. Results and Discussion

3.1. SEM/EDS characterization

Fig. 3 shows the SEM micrographs of the as-printed top surfaces of the test structures after the Ti64 deposition. The images indicated fusion between the adjacent raster scan paths, confirming that the choice of print settings was within the appropriate operational range. The formation of surface cracks having sharp fractures and abrupt changes in direction was observed in both cases; however, the introduction of the nitinol interlayer reduced the number of surface cracks. The morphology of these cracks indicated a possible brittle failure mechanism, possibly due to the process-induced residual stress.

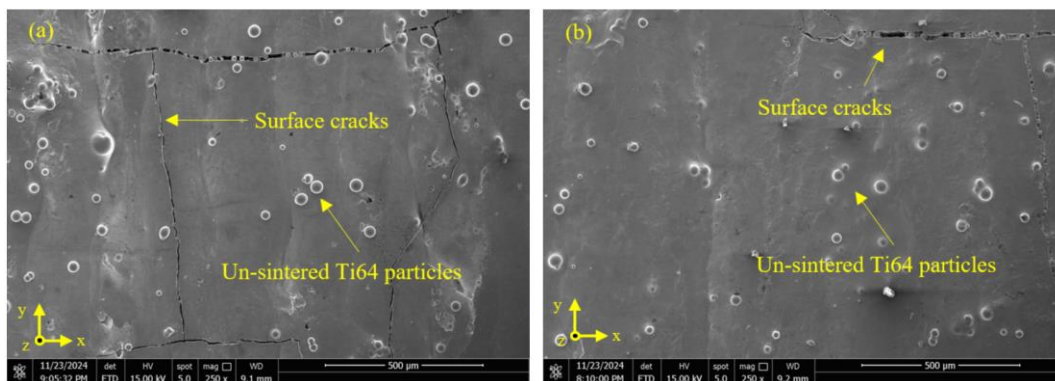
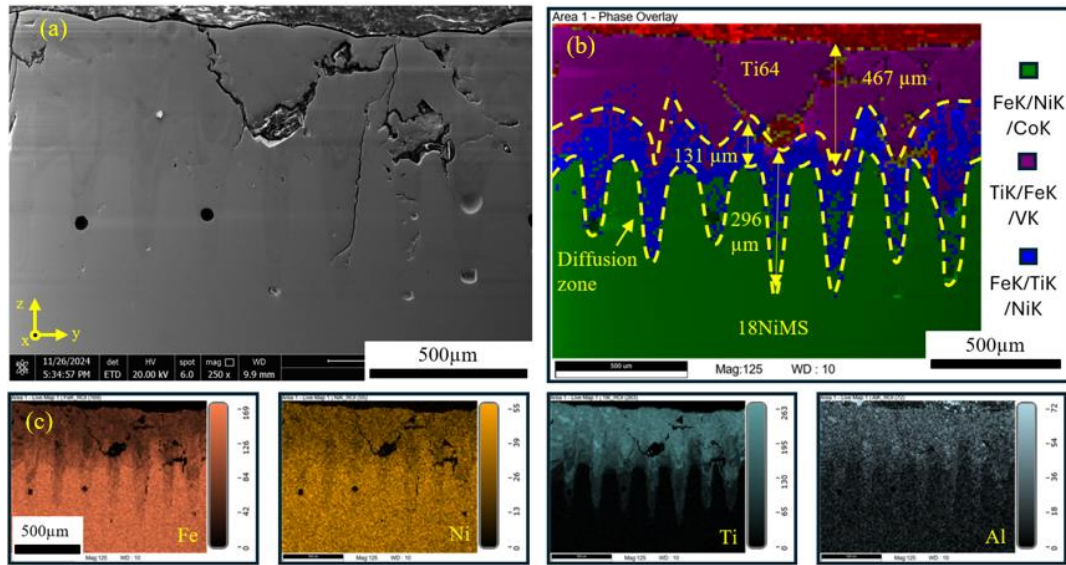
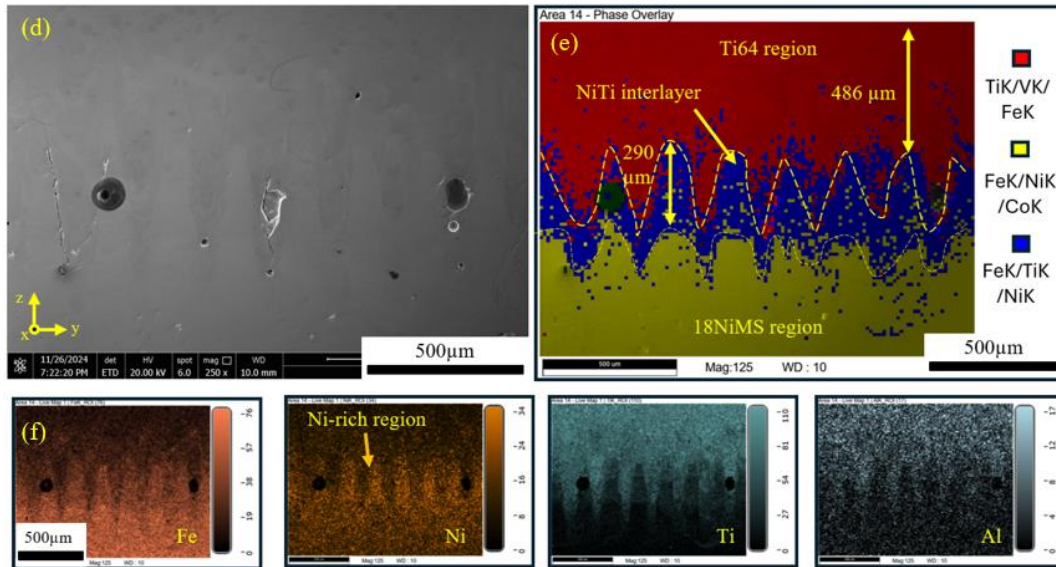


Fig. 3. Top surface morphology for (a) direct deposition and (b) deposition with interlayer.



Direct deposition



Deposition with interlayer

Fig. 4. Cross sectional data for direct deposition: (a) SEM image, (b) phase overlay map and (c) Fe, Ni, Ti, Al elemental maps; deposition with interlayer: (d) SEM image, (e) phase overlay map and (f) Fe, Ni, Ti, Al elemental maps.

Fig. 4 depicts a comparison of cross-sectional surface morphology for both sets of samples - direct deposition (top) and deposition with nitinol interlayer (bottom). Consistent with the above observations, a significant reduction in the density of cracks was observed when the nitinol interlayer was introduced. This indicated that the use of an interlayer with compatible chemistry between two layers of dissimilar metal alloys (maraging steel and Ti64) was beneficial. This is further indicated by the crack morphology observed for the direct deposition (Fig. 4 (a)), where

the cracks have penetrated through the depth of the printed Ti64 layer. The EDS maps for both cases show three distinct regions, namely 1) Fe-rich (18NiMS) region, 2) intermixed phase region, and 3) Ti-rich region (Ti64). The intermixed region is of particular interest as it represents the transition zone between the two dissimilar metal alloys. In the case of direct deposition, this intermixed region (Fig. 4 (b)-(c)) revealed Fe/Ti/Ni elemental signatures and spans approximately 131 μm -296 μm (corresponding to 3-6 layers). This could explain the presence of interfacial cracks observed along the melt pool boundary where Fe-rich and Ti-rich regions interact. Additionally, the Fe-Ti phase diagram indicates the possible formation of intermetallic compounds (IMCs) in most compositions due to limited solid solubility between these elements [7]. In the case of deposition with nitinol interlayer (Fig. 4 (d)), the density of cracks is reduced, with no surface penetrating cracks visible. The intermixed region (Fig. 4 (e)-(f)) still showed the presence of Fe/Ni/Ti elements, suggesting deeper melt pool penetration, causing intermixing between Fe and Ti phases. This indicated that the thickness of the nitinol interlayer was not sufficient to separate the 18NiMS and Ti64 regions and needs to be increased for future experiments. In addition to the above observations, both sets of samples showed the presence of spherical pores that could be attributed to the formation of keyholes, suggesting that the VED used during Ti64 deposition was relatively high. This also offered valuable insight for planning future experiments, which will be discussed in the future directions section. Further microstructural characterization was performed using XRD and EBSD measurements to gain further understanding of the intermixed region, as discussed below.

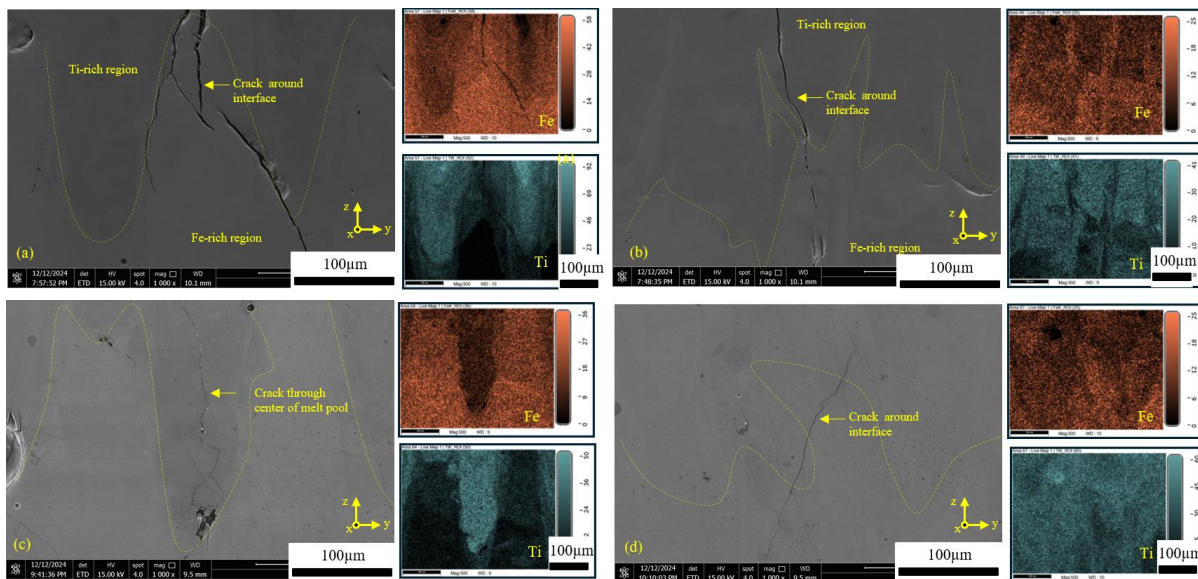


Fig. 5. High magnification SEM images and EDS maps around cracked regions: (a,b) direct deposition and (c,d) deposition with interlayer.

The specific locations of observed cracks were characterized at higher magnification as presented in Fig. 5 in order to gain further insights into possible mechanisms for their formation. In the case of direct deposition (Fig.5 (a), (b)), cracks were observed at the interfacial locations where Fe and Ti intermix directly, pointing to the possible formation of IMCs. However, very few such cracks were seen in the deposition with an interlayer, indicating reduced interaction between Fe and Ti due to the addition of the nitinol interlayer. The predominant type of crack in the deposition with an interlayer was solidification cracking, also known as hot cracking, as shown in Fig. 5 (c). These cracks were observed at the center of the Ti-rich melt pool and can be controlled by modifying the process parameters [19] as a part of the future study.

3.2. XRD analysis

XRD analysis was conducted on cross-sectional samples from both test structures, with the beam focused on the interfacial region. The collected data were then normalized by peak intensities to allow for comparative analysis between different measurements. XRD measurements were also taken on as-printed 18NiMS and Ti64 sample surfaces processed with the same parameters as listed in Tab. 2 for a baseline reference. The International Center for Diffraction Data (ICDD) database was used to identify peaks corresponding to different phases.

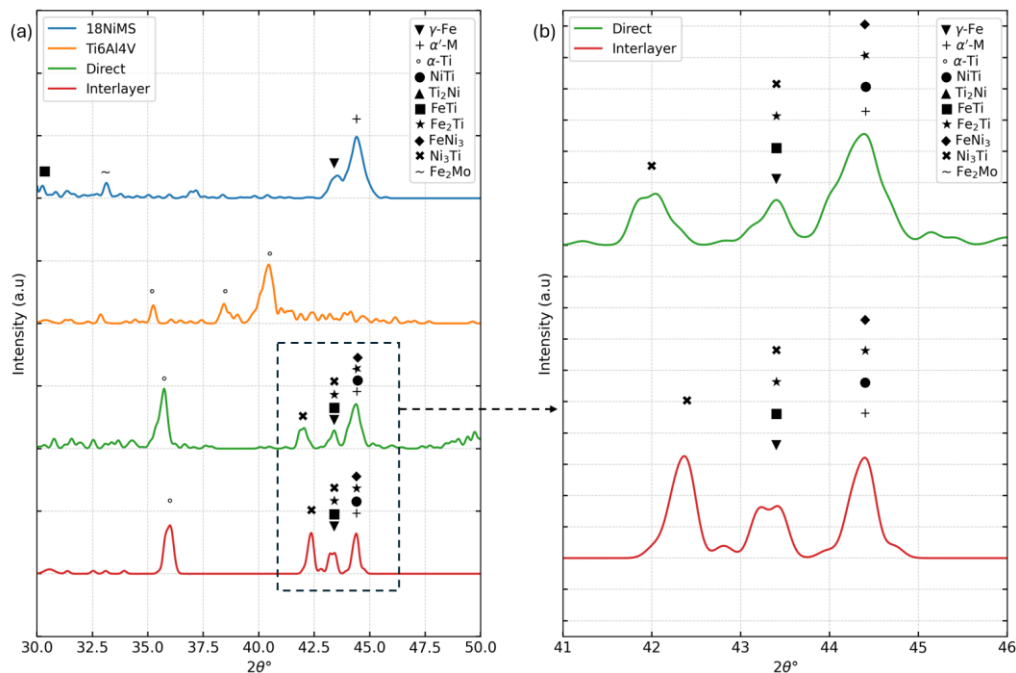


Fig. 6. (a) XRD patterns for different depositions showing formation of IMCs, (b) an inset of the region of interest for detailed view.

The XRD diffractogram for the deposited samples in the 2θ range of $30\text{--}50^\circ$ is presented in Fig. 6 (a). The reference peaks for the 18NiMS show the formation of FeTi, Fe₂Ti, γ -Fe, and α' -martensite phases, consistent with the literature reports on AM deposited 18Ni maraging steel samples with L-PBF [20]. Similarly, the reference peaks for Ti64 show the formation of the α -Ti phase [21]. The possible IMCs phases based on Fe-Ti, Fe-Ni, and Ni-Ti binary phase diagrams are FeTi, Fe₂Ti, NiTi, Ti₂Ni, Ni₃Ti, FeNi₃ [7,12,13]. A distinct phase was observed at a 2θ angle of 42.4° for both sets of test cases. This peak corresponded to the Ni₃Ti phase for the (201) plane. The XRD plot also shows the formation of γ -Fe, FeTi (110), Fe₂Ti (200), and Ni₃Ti (004) at 43.4° and α' -martensite, NiTi (111), Fe₂Ti (112), and FeNi₃ (111) at an angle of 44.4° .

To understand the effect of the addition of nitinol interlayer, the peak intensities of IMC phases were compared for both deposition types in the zoomed-in view shown in Fig. 6 (b). The Ni₃Ti phase, detected at 42.4° in the direct deposition scenario, likely resulted from the interaction between Ti and Ni from Ti64 and 18Ni maraging steel, respectively. As expected, the interaction between Ni and Ti is more prevalent due to the introduction of 55 wt.% of Ni in the interlayer, thus manifesting in higher peak intensity for Ni₃Ti as compared to the direct deposition case. Furthermore, at 44.4° , the peak intensity for the direct deposition is mainly governed by Fe₂Ti IMC rather than FeNi₃ and NiTi due to the limited Ni in 18NiMS. The addition of nitinol interlayer creates a gradient in Ti concentration while also increasing the Ni concentration across the interface, thus limiting the Fe-Ti interactions while promoting the Fe-Ni and Ti-Ni interactions. Hence, the addition of the interlayer was anticipated to suppress Fe₂Ti formation while promoting the formation of FeNi₃ and NiTi phases. The slight reduction in the peak intensity at 44.4° indicated possible replacement of Fe₂Ti IMC by FeNi₃ and NiTi IMCs. The increase in the peak intensity at 43.4° was attributed to a combined effect of the increase in the Ni₃Ti formation and the reduction in FeTi and Fe₂Ti. Introducing the nitinol interlayer thus effectively minimized the formation of detrimental Fe-Ti IMCs and replaced them with less detrimental Fe-Ni and Ti-Ni IMCs [22]. Specifically, the FeTi and Fe₂Ti phases were replaced with NiTi, Ni₃Ti, and FeNi₃ phases. Consequently, the interfacial integrity is improved when the interlayer is utilized.

3.3. EBSD Microstructural analysis

Microstructural analysis was conducted using the EBSD technique with an in-situ EDS capability to understand phase evolution and grain size distribution during the MM deposition. EBSD scans were performed at the interfacial region for both deposition types, with phase analysis guided by the possible phases identified through XRD. Interfacial cracking was observed (Fig. 7(a)) in the direct deposition. The interfacial region in Fig. 7(c) revealed the presence of Ni₃Ti and Fe₂Ti IMCs, with a thick IMC zone likely contributing to severe interfacial cracking. Additionally, Fig. 7(d) illustrates grain coarsening along the build direction from the 18NiMS region toward the Ti64 side, attributed to the lower thermal conductivity of Ti64 compared to 18NiMS.

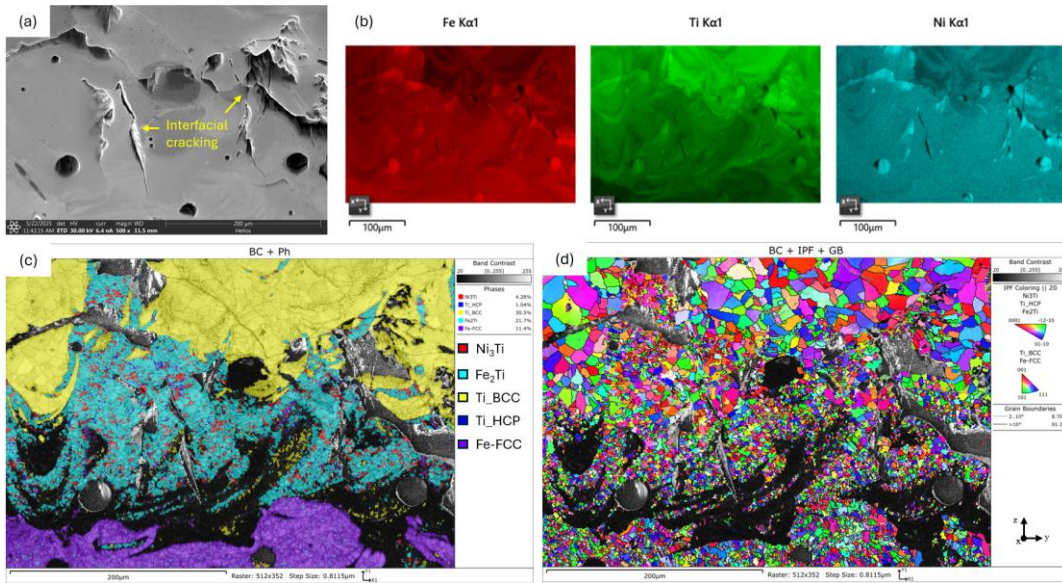


Fig. 7. EBSD microstructural analysis of direct deposition interface: (a) SEM image of the interface, (b) EDS maps, (c) phase map, and (d) grain size and orientation maps.

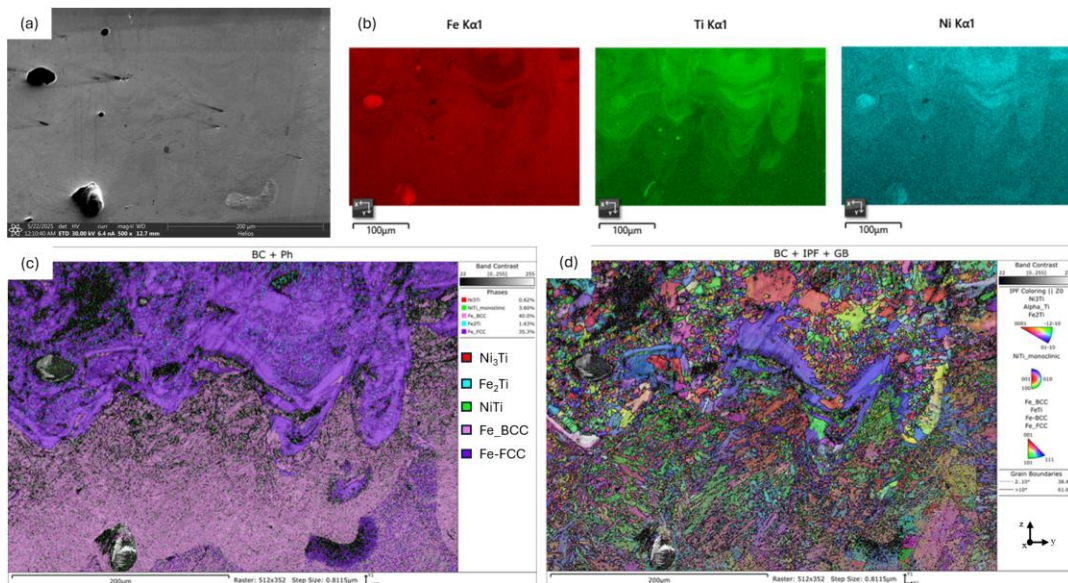


Fig. 8. EBSD microstructural analysis of deposition with interlayer depicting nitinol-18NiMS interface: (a) SEM image of the interface, (b) EDS maps, (c) phase map, and (d) grain size and orientation maps.

For the deposition incorporating the nitinol interlayer, two distinct interfacial zones were characterized: the nitinol–18NiMS interface (Fig. 8) and the Ti64–nitinol interface (Fig. 9). The SEM image in Fig. 8(a) shows a crack-free deposition of nitinol over 18NiMS, indicating sufficient chemical compatibility of nitinol with 18NiMS as compared to Ti64. As compared with the direct deposition case, significantly reduced Fe_2Ti IMC formation was observed, as shown in Fig. 8(c). On the other hand, the Ti64–nitinol interface showed both solidification cracking and interfacial cracking as shown in Fig. 9 (a). The interfacial zone in this region showed Fe_2Ti and Ni_3Ti IMC formation, resulting in interfacial cracking. The formation of Fe_2Ti IMC in this case indicated that the thickness of the nitinol interlayer was likely not sufficient to fully decouple 18NiMS and Ti64 to reduce the diffusion of Fe from 18NiMS to the Ti-rich Ti64 region. Thus, increasing the thickness of the nitinol interlayer could further reduce the detrimental Fe_2Ti IMC formation, thereby reducing the interfacial cracking. It must also be noted that both Fig. 8(d) and 9(d) depict grain coarsening along the build direction, while moving from 18NiMS to Ti64 through the nitinol interlayer due to the gradual reduction in the thermal conductivity in the build direction.

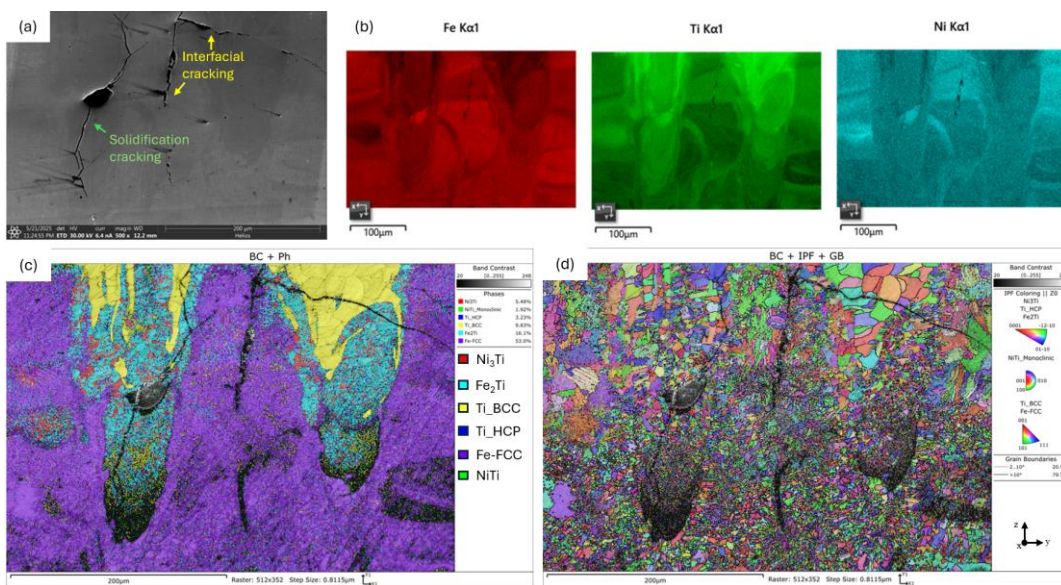


Fig. 9. EBSD microstructural analysis of deposition with interlayer depicting Ti64-nitinol interface: (a) SEM image of the interface, (b) EDS maps, (c) phase map, and (d) grain size and orientation maps.

4. Conclusions and Future Directions

This study demonstrated the feasibility of using nitinol as an interlayer to enhance the interfacial integrity of Ti64-18NiMS multi-metal structures using L-PBF. The addition of nitinol interlayer resulted in a significant reduction in defect density within the interfacial zone, which was attributed to a reduction in the direct interaction between two metal alloys (Fe-rich 18NiMS

and Ti-rich Ti64) with limited chemical compatibility. This was confirmed by the XRD analysis that indicated possible presence of detrimental FeTi and Fe₂Ti IMCs in the direct deposition case, which were replaced by the FeNi₃, NiTi, and Ni₃Ti IMCs upon introducing the nitinol interlayer. EBSD results revealed the formation of Fe₂Ti and Ni₃Ti IMCs in the interfacial zone for direct deposition, leading to interfacial cracking. For the deposition with interlayer, no cracks were observed in the nitinol-18NiMS interface due to significantly reduced IMC formation, while interfacial cracking was observed in the nitinol-Ti64 interface due to possible formation of Fe₂Ti and Ni₃Ti. Both deposition types showed grain coarsening in the build direction due to a reduction in thermal conductivity. While the interfacial integrity was enhanced by introducing nitinol interlayer chemistry, the presence of cracks in cross-sectional micrographs indicated that the process-induced thermal effects and IMCs still contribute toward suboptimal printing and thus provided important insights in the design of future experiments, as discussed below. This study establishes the foundation for understanding the influence of interlayer chemistry in enabling Fe–Ti multi-metal structures, which hold significant potential for lightweight applications in aerospace, defense, and automotive sectors.

Based on the above results, future experiments will systematically target further optimization of MM printing using nitinol interlayer including 1) increasing the thickness of the nitinol interlayer to reduce Fe-Ti interaction, and 2) exploring the role of thermal heat treatments after each stage of deposition (for example, stress relief heat treatments after 18NiMS and nitinol deposition) to promote better interfacial integrity. Additionally, a detailed and systematic parametric optimization study is planned to manufacture large-sized coupons, potentially toward studying the mechanical properties (e.g., via tensile testing, fatigue testing) of MM structures for evaluating scale-up for production.

Acknowledgments

Research was sponsored by DEVCOM US Army Research Laboratory and was accomplished under Cooperative Agreement Number W911NF-21-20059. The views and conclusions contained in this document are those of the authors and should not be interpreted as representing the official policies, either expressed or implied, of the Army Research Laboratory or the U.S. Government. The U.S. Government is authorized to reproduce and distribute reprints for Government purposes notwithstanding any copyright notation herein.

References

- [1] Zheng X, Williams C, Spadaccini CM, Shea K. Perspectives on multi-material additive manufacturing. *J Mater Res* 2021;36:3549–57.
- [2] Ferro P, Fabrizi A, Elsayed H, Savio G. Multi-material additive manufacturing: creating

- IN718-AISI 316L bimetallic parts by 3D printing, debinding, and sintering. *Sustainability* 2023;15:11911.
- [3] Fonseca DPM da, Feitosa ALM, Carvalho LG de, Plaut RL, Padilha AF. A short review on ultra-high-strength maraging steels and future perspectives. *Materials Research* 2021;24:e20200470.
- [4] Tong J, Bowen CR, Persson J, Plummer A. Mechanical properties of titanium-based Ti–6Al–4V alloys manufactured by powder bed additive manufacture. *Materials Science and Technology* 2017;33:138–48.
- [5] Andreu A, Kim S, Kim I, Kim J-H, Noh J, Lee S, et al. Processing Challenges and Delamination Prevention Methods in Titanium-Steel DED 3D Printing. *International Journal of Precision Engineering and Manufacturing-Green Technology* 2024:1–17.
- [6] Li W, Yan L, Karnati S, Liou F, Newkirk J, Tamingir KMB, et al. Ti-Fe intermetallics analysis and control in joining titanium alloy and stainless steel by Laser Metal Deposition. *J Mater Process Technol* 2017;242:39–48.
- [7] Murray JL. The Fe– Ti (iron-titanium) system. *Bulletin of Alloy Phase Diagrams* 1981;2:320–34.
- [8] Tey CF, Tan X, Sing SL, Yeong WY. Additive manufacturing of multiple materials by selective laser melting: Ti-alloy to stainless steel via a Cu-alloy interlayer. *Addit Manuf* 2020;31:100970.
- [9] Hu K, Tian Y, Jiang X, Yu H, Sun D. Microstructure regulation and performance of titanium alloy coating with Ni interlayer on the surface of mild steel by laser cladding. *Surf Coat Technol* 2024;487:130939.
- [10] Adomako NK, Noh S, Oh C-S, Yang S, Kim JH. Laser deposition additive manufacturing of 17-4PH stainless steel on Ti-6Al-4V using V interlayer. *Mater Res Lett* 2019;7:259–66.
- [11] Lee MK, Lee JG, Choi YH, Kim DW, Rhee CK, Lee YB, et al. Interlayer engineering for dissimilar bonding of titanium to stainless steel. *Mater Lett* 2010;64:1105–8.
- [12] Silman GI. Compilative Fe–Ni phase diagram with author’s correction. *Metal Science and Heat Treatment* 2012;54:105–12.
- [13] Cascadan D, Grandini CR. Structure, Microstructure, and Some Selected Mechanical Properties of Ti-Ni Alloys. *Recent Advancements in the Metallurgical Engineering and Electrodeposition*, IntechOpen London, UK; 2019, p. 1–14.
- [14] Wei S, Zhang J, Zhang L, Zhang Y, Song B, Wang X, et al. Laser powder bed fusion additive manufacturing of NiTi shape memory alloys: a review. *International Journal of Extreme Manufacturing* 2023;5:032001.
- [15] Safaei K, Abedi H, Nematollahi M, Kordizadeh F, Dabbaghi H, Bayati P, et al. Additive manufacturing of NiTi shape memory alloy for biomedical applications: review of the LPBF process ecosystem. *Jom* 2021:1–16.
- [16] Acevedo R, Sedlak P, Kolman R, Fredel M. Residual stress analysis of additive manufacturing of metallic parts using ultrasonic waves: State of the art review. *Journal of*

- Materials Research and Technology 2020;9:9457–77.
- [17] Chen W, Xu L, Han Y, Zhao L, Jing H. Control of residual stress in metal additive manufacturing by low-temperature solid-state phase transformation: An experimental and numerical study. *Addit Manuf* 2021;42:102016.
 - [18] Carson C. Heat treating of maraging steels. *Heat Treating of Irons and Steels*, ASM International; 2014, p. 468–80.
 - [19] Sabzi HE, Maeng S, Liang X, Simonelli M, Aboulkhair NT, Rivera-Díaz-del-Castillo PEJ. Controlling crack formation and porosity in laser powder bed fusion: Alloy design and process optimisation. *Addit Manuf* 2020;34:101360.
 - [20] Ferreira DFS, Miranda G, Oliveira FJ, Oliveira JM. Conventionally and SLM-manufactured 18Ni300 steel: mechanical and tribological behaviour in dry sliding against PP40 composite. *The International Journal of Advanced Manufacturing Technology* 2022;122:1245–58.
 - [21] Panin A, Kazachenok M, Kolmakov A, Chizhik S, Heifetz M, Chugui Y. Microstructure and mechanical behaviour of additive manufactured Ti–6Al–4V parts under tension. *EPJ Web Conf*, vol. 221, EDP Sciences; 2019, p. 1037.
 - [22] Shiue RK, Wu SK, Chan CH, Huang CS. Infrared brazing of Ti-6Al-4V and 17-4 PH stainless steel with a nickel barrier layer. *Metallurgical and Materials Transactions A* 2006;37:2207–17.